ЖЭТФ, 2015, том 147, вып. 6, стр. 1098–1112

SILICON AS A VIRTUAL PLASMONIC MATERIAL: ACQUISITION OF ITS TRANSIENT OPTICAL CONSTANTS AND THE ULTRAFAST SURFACE PLASMON–POLARITON EXCITATION

P. A. Danilov [a,b], **A. A. Ionin** [a], **S. I. Kudryashov** [a,b*], **S. V. Makarov** [a], **A. A. Rudenko** [a], **P. N. Saltuganov** [c], **L. V. Seleznev** [a], **V. I. Yurovskikh** [a,b], **D. A. Zayarny** [a], **T. Apostolova** [d]

[a] *Lebedev Physical Institute*
119991, Moscow, Russia

[b] *National research nuclear university "MEPhI" (Moscow Engineering Physics Institute)*
115409, Moscow, Russia

[c] *Moscow Physico-Technical Institute "MIPT" (State University)*
141700, Dolgoprudny, Moscow Region, Russia

[d] *Institute for Nuclear Research and Nuclear Energetics, Bulgarian Academy of Sciences*
1784, Sofia, Bulgaria

Received October 25, 2014

Ultrafast intense photoexcitation of a silicon surface is complementarily studied experimentally and theoretically, with its prompt optical dielectric function obtained by means of time-resolved optical reflection microscopy and the underlying electron–hole plasma dynamics modeled numerically, using a quantum kinetic approach. The corresponding transient surface plasmon–polariton (SPP) dispersion curves of the photo-excited material were simulated as a function of the electron–hole plasma density, using the derived optical dielectric function model, and directly mapped at several laser photon energies, measuring spatial periods of the corresponding SPP-mediated surface relief nanogratings. The unusual spectral dynamics of the surface plasmon resonance, initially increasing with the increase in the electron–hole plasma density but damped at high interband absorption losses induced by the high-density electron–hole plasma through instantaneous bandgap renormalization, was envisioned through the multi-color mapping.

DOI: 10.7868/S0044451015060038

1. INTRODUCTION

Semiconductors are prospective "virtual" materials for active plasmonics, requiring intense ultrafast (femtosecond, fs) photo-injection of different carrier densities — from rare gas of separate electron–hole pairs to their dense "plasma fluid" (electron–hole plasma, EHP) — to demonstrate their broad (far-IR–UV) spectral tunability for promising plasmonic, optical switching, THz-related, and other applications [1–4]. Although the dielectric function spectra for unexcited semiconductors are of common knowledge [5], the advanced use of photo-excited semiconductors in plasmonics undermines a profound knowledge of their broad-range dielectric function spectra for a range of photo-injected EHP densities $\rho_{eh} \approx 10^{16}$–$10^{22}$ cm^{-3}. While experimental time-resolved acquisition of transient optical constants of photo-excited semiconductors is rather trivial at low EHP densities ($\rho_{eh} < 10^{21}$ cm^{-3}) [6, 7], it becomes a challenging task at higher ρ_{eh}, since a strong modulation of their dielectric function $\varepsilon = \varepsilon_1 + i\varepsilon_2$ is expected for $\rho_{eh} > 10^{21}$ cm^{-3}, when both photo-induced intraband and interband electronic transitions are additionally affected by a significant prompt electronic bandgap renormalization [8–15].

Experimental studies of transient optical-range dielectric functions (ODF) of strongly photo-excited semiconductors are rather scarce [11–23] (see the historical overview of early works in Ref. [23]), represen-

---

[*] E-mail: sikudr@sci.lebedev.ru

ting transient ODFs, if any, just at a few visible probe wavelengths (400–800 nm) as a function of the laser fluence F or intensity I, not ρ_{eh}. In the first time-resolved study [16], the photo-generated EHP density $\rho_{eh} \sim 10^{21}$ cm^{-3} on a bulk Si surface was evaluated from its transient reflectivity changes at the 625 nm fs-laser wavelength, using a simple Drude model. Later, similar research was performed in Ref. [17] under strong 625 nm fs-laser excitation conditions, yielding the EHP with $\rho_{eh} \sim 10^{22}$ cm^{-3} estimated according to a similar Drude model. An accurate study was undertaken by Downer et al. [18], by looking at the time-resolved transmission of 625 nm fs-laser pulses through a submicron silicon-on-insulator film to envision the basic two-photon absorbance at moderate fs-laser intensities (less than 0.3 TW/cm^2) and an unidentified drastic rise of a much stronger absorption (approximately 10^5 cm^{-1}) at slightly higher intensities. A similar large transient ODF modulation was observed in Si, GeSb, and GaAs [11], related to the prompt electronic bandgap renormalization. In this regard, a linear relation between electronic bandgap shrinkage and the EHP density was experimentally demonstrated later in Te Ref. [13]. Then, another detailed time-resolved optical reflection microscopy research on bulk Si used the analysis of experimental reflectivity dependences on laser fluence, accompanied by a comprehensive modeling of its dielectric function at minor bandgap shrinkage and the absent EHP screening, to demonstrate a two-photon EHP generation mechanism up to $\rho_{eh} \sim 10^{22}$ cm^{-3} [19], although without any expected Auger recombination as a ionization limiting mechanism [15, 16, 24]. With the key Auger recombination process ignored in the analysis, time-resolved reflection studies on silicon have resulted in high EHP densities approaching 10^{23} cm^{-3} [20]. Finally, in Ref. [22], the authors reported ultrahigh $\rho_{eh} \sim 10^{22}$–10^{23} cm^{-3} and absolute ODF amplitudes up to 200 at the 1240 nm pump/probe wavelengths in the fluence range between melting and ablation thresholds of silicon, invoking additional non-Fresnel optical analysis of EHP surface gradients. Overall, the previous basic experimental studies of dense EHP photo-generation ρ_{eh} versus the laser fluence F or laser intensity I, in each case missing some important physical effects in their analysis, provide not only a rather contradictory physical picture of the photogeneration and EHP relaxation dynamics in semiconductors [11–23] but also rather unreliable output ρ_{eh} magnitudes ($5 \cdot 10^{21}$–10^{23} cm^{-3}) even for quite similar photo-excitation conditions.

Moreover, the present different theoretical descriptions of such ultrafast photogeneration and relaxation dynamics of dense EHP are also not satisfactory. Typically, a nonlinear partial differential equation is used, where the rates of carrier generation, carrier diffusion, and Auger recombination are considered with the last term not dynamically depending on ρ_{eh} and the bandgap renormalization effect not taken into account for $\rho_{eh} \sim 10^{22}$ cm^{-3} [19, 20]. Alternatively, energy balance equations for the electron and lattice systems are used [20, 25, 26]. Another approach is a two-temperature model (TTM) description based on a semiclassical Boltzmann equation [27], upgraded later to an improved TTM model coupled with a rate equation for one- and two-photon carrier generation, diffusion, and Auger recombination, but again disregarding the dynamical EHP effects on the Auger recombination rate and band-gap renormalization [28, 29]. Later, the same model was coupled with molecular dynamics to describe carrier–lattice heat exchange [30]. Finally, more accurate nonequilibrium theoretical descriptions, based on the Boltzmann equation or kinetic Monte Carlo simulations, were also recently applied for the modeling of ultrafast EHP photo-excitation and relaxation dynamics in semiconductors [31–34], still ignoring the essential dynamical interplay between EHP photogeneration and instantaneous changes of optical and electronic properties of such strongly photo-excited materials.

The main reasons of these uncertainties and controversies are related, in our opinion, to improperly accounting for various basic electronic processes in a dense EHP driven by intense ultrashort laser pulses during its ultrafast photoexcitation and relaxation in semiconductors and dielectrics. The whole set of these processes in a dense EHP ($\rho_{eh} > 10^{21}$ cm^{-3}) includes (but is not limited by) band-filling [11, 14, 18, 19], EHP screening of multi-particle interactions (e. g., Auger recombination [24]), static ion–core potentials [8–10], inter-valley electron–phonon scattering [22], and intense ultrafast excitation of coherent optical phonons [13], prompt electronic and delayed phonon-mediated band spectrum renormalization [8–15, 19], as well as the consequent increase in kinetic rates for linear and nonlinear photo-ionization cross sections [14, 35], impact and tunnel ionization rates [14], Auger recombination [14], electron emission, and surface charging [15]. Some of the mentioned phenomena were not even explicitly revealed in the previous experiments, and that is why their relative contributions are not yet evaluated. But in the highly nonlinear EHP dynamics, any underestimation or overestimation for some of these counterbalancing effects results in a distorted physical picture and large resulting errors in the basic parameters, the EHP density and temperature, intraband absorption, and deposited energy density. Specifically, the important factor of prompt electronic bandgap renormalization [8–15] was often disregarded in the preceding theoretical models aimed to fit the transient optical reflectivity of such materials [16–23], yielding unbalanced reflectivity analysis algorithms and, hence, overestimated common Drude contributions to the dielectric function [17, 19, 21, 22]. As a result, strong ultrafast photo-excitation of semiconductor surfaces, as a primary step of many fs-laser ablative nano- and micro-machining technologies, remains not well understood and predictable.

In particular, an expected prospective regime of fs-laser surface nanostructuring of strongly photoexcited semiconductors, invoking their surface plasmon resonance (SPR, strongly dissipative mode) through prompt constructive interference of the transverse electric field of an incident laser wave with the longitudinal electric field of a laser excited short-wavelength surface plasmon wave to produce nanoscale surface relief gratings has been neither predicted, nor yet realized. By contrast, presumably multi-shot fs-laser submicrometer-scale structuring of their surfaces, mediated by near-wavelength polaritonic-like surface waves (long-propagation modes), was commonly revealed at very different photoexcitation conditions [36–41]. Furthermore, the related extensive theoretical modeling of transient ODF and corresponding prompt SPP dispersion curves [38, 39] was limited by rather trivial regimes of moderate photo-excitation ($|\varepsilon_1| \gg \varepsilon_2$) [42], thereby ignoring the important SPR region with $|\varepsilon_1| \sim \varepsilon_2$ [43]. Only recently, one comprehensive model was proposed for accurate experimental acquisition of ODF and EHP densities in photo-excited insulators [14, 15], which accounts for basic features of dense EHP and its dynamics, involving optical carrier mass dispersion and renormalization, band-filling effects, isotropic bandgap renormalization, and screening effects. This makes it a versatile tool for pioneering, enlightening full-scale simulations of surface plasmon–polariton dispersion curves of strongly photo-excited semiconductors over a broad IR–UV spectral range.

In this paper, we report high-fluence ultrafast laser photo-excitation of a silicon surface to probe multiphoton photo-generation and recombination of the electron–hole plasma, as well as prompt electronic bandgap renormalization. These processes were numerically modeled using a quantum kinetic approach, based on a solution of a kinetic Boltzmann equation. The derived model dielectric function of photo-excited silicon was used to simulate its surface plasmon–polariton dispersion curves from near-IR to UV, which were experimentally mapped at different photoexcitation conditions by measuring spatial periods of surface plasmon–polariton-mediated surface relief gratings.

2. EXPERIMENTAL SETUP AND TECHNIQUES

2.1. Time-resolved optical reflection microscopy

In the experiments, we used a commercial 0.45 mm thick, atomically flat undoped silicon Si(100) wafer with a few-nanometer-thick native oxide layer, arranged on a three-dimensional motorized translation micro-stage under PC control and raster-moved from laser shot to shot to expose its fresh surface spots (Fig. 1). Its single-shot laser irradiation (one laser pulse per surface spot) at a repetition rate of 10 Hz was provided by single IR (800 nm) Ti:sapphire laser pulses in the TEM_{00} mode with the FWHM (full-width at half-maximum) duration $\tau_{pump} \approx 100$ fs and pulse energies up to 1.5 mJ, using a triggered electro-mechanical shut-

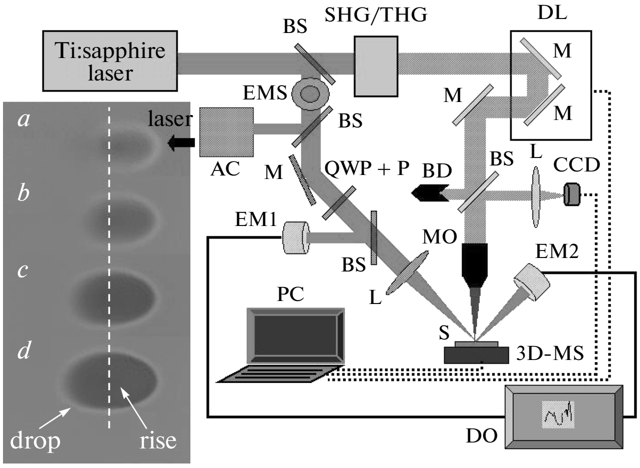

Fig. 1. Experimental setup: BS — beam splitter, AC — autocorrelator, QPW+GPP — energy attenuating set of a half-wave plate and a Glan-prism polarizer, EM1,2 — thermocouple energy meters, M — mirror, L — focusing silica lenses, HG — second and third harmonics generator, DL — optical probe delay line, CCD — charge-coupled device camera, BD — beam dump, DO — digital oscilloscope, 3D-MS — three-dimensional motorized micro-stage, PC — laptop for data acquisition and hardware control. Insets: images (500 μm × 300 μm) of a single-shot fs-laser excited Si surface spot at $F = 1.4$ J/cm^2 for $\Delta t = -0.1$ (a), 0 (b), +0.1 (c), +0.2 ps (d) with the dashed line showing their centered spatial cross sections used for the fluence conversion

ter. The pump pulse energy was reduced in these experiments using a combination of a half-wave plate and a Glan-prism polarizer, to the minimum level slightly above 0.2 mJ to avoid the laser beam degradation due to its self-focusing in air and air plasma scattering/refraction (the critical power at the wavelength of about 3 GW [44], i.e., approximately 0.3 mJ for the 100 fs laser pulses).

The fs-laser pump pulses were focused in p-polarization at the angle of 45° by a silica lens (focal distance $f = 500$ mm) into a small focal spot (with the Gaussian main ellipse $1/e$-radii $\varnothing_{1/e,x} \approx 0.10$ mm and $\varnothing_{1/e,y} \approx 0.05$ mm) on the surface of the Si sample, arranged in front of a smaller aperture of a probe-line microscope objective (NA = 0.37) (Fig. 1). The time-resolved optical reflection microscopy arrangement described elsewhere [12, 14, 15, 19, 20] used a strong small pump beam at 800 nm and a temporally delayed (in this work, $\Delta t = -0.1$–$+0.2$ ps with the accuracy of 0.05 ps), fifty times weaker large frequency-doubled probe beam at 400 nm (FWHM $\tau_{probe} \approx 100$ fs), provided by second harmonic generation in a 1.5 mm thick BBO crystal in a harmonics generator. Zero-time delay $\Delta t = 0$ was assigned to the instant when the pump and probe pulse peaks coincide exactly in the sample plane. The initial sample reflectivity $R_0 = 0.49 \pm 0.01$ was calibrated using an aluminum mirror (the normal-incidence reflection at 400 nm is about 0.92), in agreement with its tabulated value of approximately 0.488 [5]. The incident fluence calibration, providing the peak surface fluence F up to 1.5 J/cm^2 as a function of the incident energy and the abovementioned Gaussian beam parameters, was performed by means of an optical microscope to measure the main radii of the resulting ablative surface craters.

2.2. Surface nanostructuring

Multi-shot surface structuring of the silicon wafer was performed in ambient air by 744 nm, 100 fs Ti:sapphire or 515/1030 nm, 200/300 fs Yb:fiber laser (Satsuma, Amplitude Systemes) pulses focused by a 35 mm spherical silica lens at the normal incidence onto its surface. The wafer was arranged onto the three-dimensional motorized translation micro-stage and irradiated at different incident peak fs-laser fluences F and exposure pulse numbers N, through its raster-scanning in a number of lines. Surface topography of the resulting structured spots was characterized by a field-enhanced scanning electron microscope (FE SEM, JEOL 7001F) with a magnification up to 500000 in the relief SEM mode.

3. MODELING

As mentioned in the Introduction, transient photo-excitation and nonequilibrium relaxation dynamics of electron–hole plasma (EHP) can be adequately described by a microscopic model that treats the evolution of the carrier distribution function explicitly. In this paper, such a description is proposed using a quantum kinetic approach presented below.

The quantum kinetic formalism was previously developed in Ref. [45], and later was refined in the succeeding work [14] to describe microscopic processes occurring during the ultrashort laser pulse interaction with a GaAs surface. Its relevant terms and corresponding parameters used in our calculations for Si are briefly described below.

Compared to direct-gap GaAs, the indirect-band-gap Si semiconductor has a many-valley conduction band with elliptical energy surfaces and a degenerate valence band with heavy and light holes, and a reduced two-band model with spherical energy surfaces is used following Ref. [46]. Photo-ionization (PI), impact ionization (II), and Auger recombination (AR) dynamics in the photo-excited GaAs were modeled using the set of equations described elsewhere [14]. In this paper, two-photon absorption across the band gap is given by the expression [47, 48]

$$S_{abs} \propto \frac{2\pi}{\hbar}\left|\frac{F_k^2}{\hbar\Omega - E_k^e - E_k^h - E_G}\right|^2 \times \\ \times \frac{2F_k/\pi}{(2\hbar\Omega - E_k^e - E_k^h - E_G)^2 + 4|F_k|^2}, \tag{1}$$

where

$$|F_k|^2 \approx \frac{e^2 E_{0L}^2}{m_0\Omega}\left(\frac{m_0}{m_e^*} - 1\right)\frac{E_G(E_G + \Delta_0)}{2(E_G + 2\Delta_0/3)}. \tag{2}$$

Phonon-assisted Auger recombination was described following Refs. [49, 50].

In these numerical calculations the following parameters were chosen: the variable laser intensity (fluence) $I_L = 0.1$–10 TW/cm^2 (0.01–1 J/cm^2) for the pulse duration (FWHM) $\tau_p = 100$ fs, the initial bandgap energies (without the BGR effect) at the lattice temperature $T = 300$ K: $E_{G,0} \approx 1.12$ eV (indirect bandgap) and $E_{G,0} \approx 3.4$ eV (direct bandgap), the spin–orbit splitting of the Si bulk semiconductor $\Delta_0 = 0.6$ eV, the carrier (electron and hole) effective masses $m_e^* = 0.26 m_0$ and $m_h^* = 0.31 m_0$, where m_0 is the free electron mass, the relative high-frequency (optical) and low-frequency (static) dielectric constants $\varepsilon(\infty) = 13.5$ and $\varepsilon(0) \approx 12$, and the optical phonon energy $\hbar\omega_{LO} = 63$ meV. The charge neutrality condition $\rho_e = \rho_h$ was also assumed.

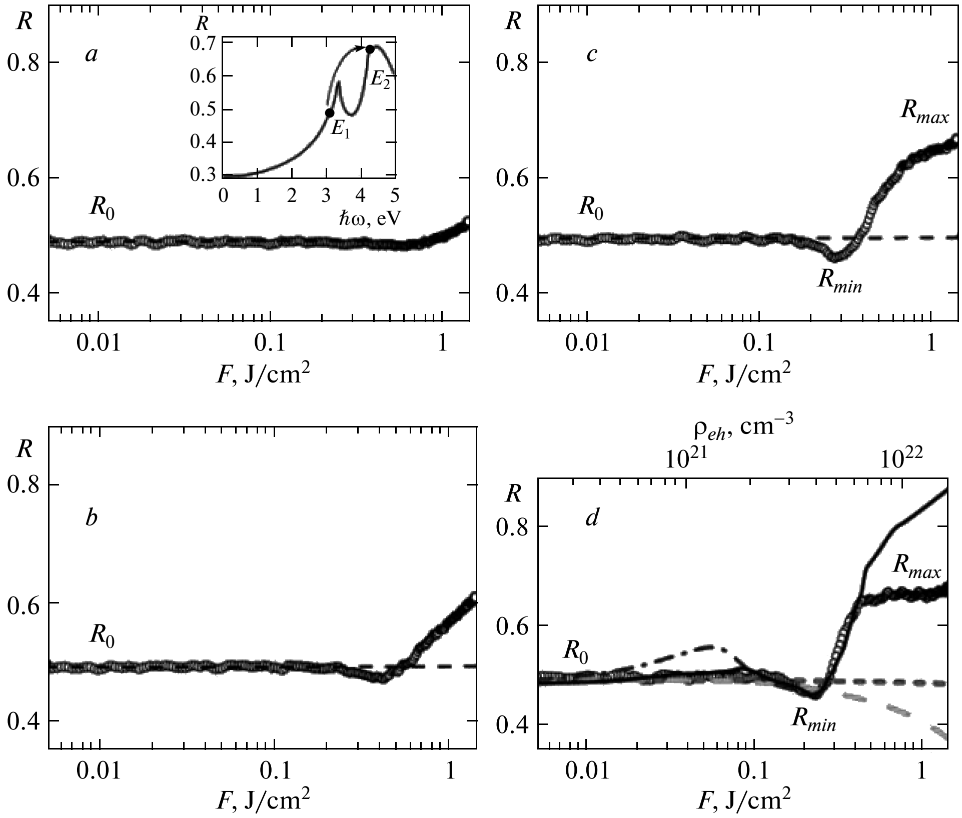

Fig. 2. Experimental probe reflectivity dependences $R(F)$ (light circles, left/right and bottom axes) at different delay times $\Delta t = -0.1$ ps (a), 0 ps (b), $+0.1$ ps (c), $+0.2$ ps (d). In figure (d), the dotted, dashed, dash-dotted, and continuous curves R(ρ_{eh}) (left/right and top axes) respectively represent 1) the pure Drude model, 2) the Drude model with EHP screening, 3) the Drude model with screening and bandgap renormalization (BGR), and 4) the Drude model combined with EHP screening, BGR and band filling. The magnitudes R_0, R_{min}, and R_{max} correspond to the initial Si reflectivity (dashed lines in a–c), the minimum and maximum reflectivity of the photo-excited material. Inset: reflectivity spectrum of unexcited silicon with the arrow showing the BGR-driven transition between the unexcited state (the initial point at 3.1 eV) and the final excited state at 4.3 eV, corresponding to R_{max} (from Ref. [5])

The prompt electronic renormalization of the direct gap in silicon (approximately 3.4 eV) in the vicinity of the Γ and L points was modeled similarly to GaAs [10] and in agreement with previous calculations of the electronic renormalization in silicon [9] under the assumption that the total valence electron density in the tetravalent material is about $2 \cdot 10^{23}$ cm^{-3} [51].

4. RESULTS

4.1. Transient Si reflectivity

The silicon surface images captured using the time-resolved optical reflection microscopy setup in Fig. 1 at different instants during the 800 nm pump pulse demonstrate a number of typical prominent temporally and spatially resolved probe reflectivity features [11–22] on the photo-excited Si surface for such short delay times (Fig. 1, insets a–d). Here, the photo-excited spot temporally extending from a semi-elliptical to a complete elliptical one appears at shorter delay times from the right to the left in the central fs-laser pumped region because of the oblique (45°) incidence of the fs-laser pump pulse from the right size, as shown by the thick dark arrow, approaching the surface first by its right edge.

Also, with the complex refractive index of Si at 800 and 400 nm being $n(800\text{ nm}) = 3.70 + 0.007i$ and $n(400\text{ nm}) = 5.57 + 0.387i$ [5], the probe penetration depth $\delta(400\text{ nm})$ is much smaller than the pumping depth $\delta(800\text{ nm})$, ensuring the probing of the nearly homogeneously excited, Fresnel-like region near the Si surface.

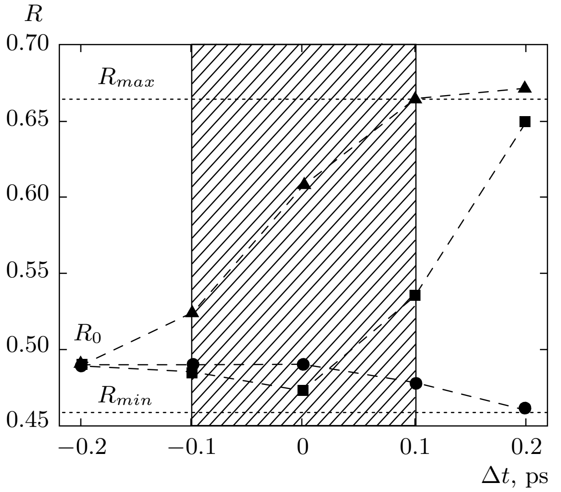

Fig. 3. Transients $R(\Delta t)$ for $F = 0.25$ (circles), 0.45 (squares), 1.4 J/cm^2 (triangles) with the shadowed area showing the reference probe pulse full width. Zero-time delay $\Delta t = 0$ ps was established as the instant when the pump and probe pulse peaks coincide exactly in the sample plane

Qualitatively, at small delay times, the revealed transient reflectivity features were as follows: 1) an initial ultrafast dip of the probe reflectivity transients below the initial value $R_0 \approx 0.49$ (Fig. 1*a*) to the minimum level $R_{min} = 0.461 \pm 0.005$, 2) a subsequent monotonous increase of R (Fig. 1*b*) until its saturation starting at $R_{max} \approx 0.67$ and extending to 0.68 (Fig. 1*c,d*).

In detail, these probe reflectity features appear more clearly on the fluence dependences $R(F)$ in Fig. 2, exhibiting the following features at these few time slices with the 0.1 ps intervals: a) a small initial positive increase of R to 0.53 for $F > 0.8$ J/cm^2 ($\Delta t = -0.1$ ps), b) a small decrease to 0.485 for $F > 0.23$ J/cm^2 and then a much higher increase to 0.61 for $F > 0.45$ J/cm^2 ($\Delta t = 0$), c) a large dip to R_{min} for $F > 0.16$ J/cm^2 with the subsequent rapid increase to R_{max} for $F >$ > 0.4 J/cm^2 ($\Delta t = 0.1$ ps) and, finally, d) a similar initial dip to R_{min} for $F > 0.13$ J/cm^2 with the subsequent step to saturation at R_{max} for $F > 0.45$ J/cm^2 ($\Delta t = 0.2$ ps).

The temporal dynamics of these features is presented in Fig. 3 for three (low, medium, and high) fluence values, indicating different dynamics of the EHP-driven optical changes on the photo-excited Si surface. In particular, at $F \approx 1.4$ J/cm^2, the probe reflectivity saturates at the level R_{max} at $\Delta t = +0.1$ ps, while at $F \approx 0.25$ J/cm^2, the reflectivity minimum R_{min} is achieved later, at $\Delta t = 0.2$ ps. In the intermediate case ($F \approx 0.45$ J/cm^2), the reflectivity passes the minimum at $\Delta t = 0$ and then almost approaches R_{max} at $\Delta t = 0.2$ ps. Accounting for the finite probe pulsewidth of approximately 0.1 ps (FWHM), we can conclude from these dynamics that the EHP density and the resulting EHP-driven optical changes on the Si surface at $\Delta t = 0$ saturate at high fluences $F \leq 1.4$ J/cm^2 (arbitrarily, in the plateau region at $R_{max} \approx 0.64$–0.68), while at lower fluences such variation of the EHP-driven optical changes, as well as the monotonous increase in the EHP density, continues until the end of the pump pulse ($\Delta t = 0.1$ ps) (see Sec. 5.1 for a discussion of the EHP dynamics). The presented pump/probe delay time assignment is quantitatively consistent with the consequent appearance of the different pump beam edges at the different instants along the horizontal line in Fig. 1 (e. g., there is almost no any reflectivity change in the pump beam center $\Delta t = -0.1$ ps, when the probe pulse comes 0.1 ps ahead of the pump pulse). Meanwhile, to account for the pump/probe pulsewidth convolution effect on the acquisition of EHP dynamics on the photo-excited silicon within the pump pulse at the key instants $\Delta t = 0$ (the pump peak intensity) and +0.1 ps (the end of the pump pulse) in our fitting analysis, the reflectivity dependence $R(F)$ was chosen in Fig. 2 at $\Delta t = 0.2$ ps (the “effective” $\Delta t = 0.1$ ps).

4.2. Surface nanostructuring

Multi-shot ($N \approx 3$–10^3 pulses) fs-laser dry nanostructuring of an atomically smooth Si(100) commercial wafer surface by the linearly polarized 744 nm fs-laser pulses resulted in one-dimensional surface gratings with their ridges perpendicular to the laser polarization vector (the “normal” gratings [23, 52]) and the periods Λ_{744}, varying depending on N and F. The observed cumulative dependence $\Lambda(N)$ is well known [53–55], with the corresponding ripple periods Λ decreasing by 30 % for larger N due to the resulting increase in the ripple depth [55]. By contrast, the fluence dependence is more related to photo-excitation conditions, exhibiting $\Lambda_{744,min}(N \approx 100) = 0.42 \pm 0.01$ μm at the local fluence $F \approx 0.15$ J/cm^2 (Fig. 4*a*), i. e., just slightly above the nanostructuring threshold $F_{744} \approx 0.13$ J/cm^2, while at higher fluences $F > 0.2$ J/cm^2, more coarse (near-wavelength) normal gratings with the period $\Lambda_{744,max}(N \approx 100) = 0.65 \pm 0.05$ μm were observed (Fig. 4*c*). This rising trend for Λ_{744} as F increases is in agreement with the previous experimental observations [54, 56].

Likewise, multi-shot surface ripples were gener-

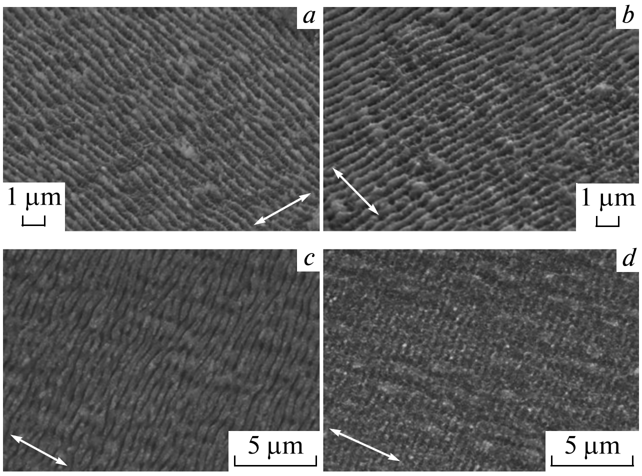

Fig. 4. SEM images of ripples generated on the silicon surface by 744 nm (1.68 eV) fs-laser pulses at $N = 100$ and different fluences F [J/cm^2]: a — 0.15, b — 0.2, c — 0.3, and d — 0.4. The bilateral arrows show the laser polarization

ated on a silicon surface at other laser wavelength of 1030 and 515 nm (Fig. 5). Compared to 744 nm fs-laser pulses, the only near-wavelength ripples with $\Lambda_{515} \approx 0.50 \pm 0.04$ μm ($N = 3$) were produced at the 515 nm wavelength above the nanostructuring threshold $F_{515}(N = 3) \approx 0.3$ J/cm^2 (Fig. 5a). By contrast, at the 1030 nm wavelength, a whole spectrum of ripple periods Λ_{1030} was observed (Fig. 5b–d), depending not only on N (in the range 0.7–1 μm, i. e., within the abovementioned 30 % cumulative decrease), but also (almost twice) on the laser fluence, exhibiting the lower-fluence finer ripples at the very nanostructuring threshold $F_{1030}(N = 30\text{–}300) \approx 0.5$ J/cm^2 (Fig. 5d; see the finer ripples slightly above the threshold fluence at the laser spot periphery and more coarse ripples at higher F closer to the central crater).

5. DISCUSSION

The experimental time-resolved reflection data and the SEM images of the fs-laser generated surface ripples provide some enlightening insights into the electronic dynamics, transient optics, and plasmonics of such fs-laser photo-excited Si surfaces.

5.1. Ultrafast optical and electronic dynamics on a photo-excited Si surface

The observed complex time- and fluence-dependent reflectivity dynamics can be understood taking into account that such a bipolar reflectivity modulation is related to the transient EHP density variation, through its basic intraband and interband contributions to the ODF [11–22]. Specifically, the observed reflectivity dip can be related to an optically driven "insulator–conductor" transition in semiconductors, when the bulk EHP frequency passes through the probing frequency, with a subsequent reflectivity increase for stronger ionized materials through their intraband electronic transitions [16–22]. Additionally, for silicon [12, 15] and other materials [11, 13, 14], the same reflectivity trends can be related to a strong prompt EHP-driven isotropic renormalization of their direct bandgap by $\delta E_{G,e} = E_{G,0} - E^*_G$, resulting in a drastic enhancement of the interband transitions. Such basic consideration of the EHP dynamics envisions the demonstrated probe reflectivity changes and enables the assignment of absolute Δt values (see the details below).

During the fs-laser photoexcitation of a silicon surface, its transient ODF ε^* can be written as a function of ρ_{eh} as a sum of interband- and intraband-transition based terms [14, 15, 19]

$$\varepsilon^*(\omega, \rho_{eh}) = \varepsilon_{IB}(\omega^*)\left(1 - \frac{\rho_{eh}}{\rho_{bf}}\right) - \frac{\omega_{pl}^2(\rho_{eh})}{\omega^2 + 1/\tau_e(\rho_{eh})^2}\left(1 - \frac{i}{\omega\tau_e(\rho_{eh})}\right), \qquad (3)$$

where the prompt ρ_{eh}-dependent bandgap shrinkage effect on the interband transitions is accounted by the spectral ODF dependence with the effective photon frequency $\omega^* = \omega[1 + \Theta\rho_{eh}/\rho_{bgr}]$. Here, the characteristic renormalization EHP density is $\rho_{bgr} \approx 1 \cdot 10^{22}$ cm^{-3} [15], typically about 5 % of the total valence electron density (approximately $2 \cdot 10^{23}$ cm^{-3} in Si) to provide the ultimate 50 % electronic direct bandgap renormalization [10], i. e., $\Theta \approx 1.7$ eV of the effective minimal gap of about 3.4 eV in silicon [5, 51], while ρ_{bf} is the characteristic band capacity of the specific photoexcited regions of the first Brillouine zone in the k-space (e. g., $\rho_{bf}(L) \approx 4 \cdot 10^{21}$ cm^{-3} for L-valleys and $\rho_{bf}(X) \approx 4.5 \cdot 10^{22}$ cm^{-3} for X-valleys in Si), affecting interband transitions via the band-filling effect [11, 14, 15, 18, 19]. The bulk EHP frequency ω_{pl} is defined as

$$\omega_{pl}^2(\rho_{eh}) = \frac{\rho_{eh}e^2}{\varepsilon_0\varepsilon_{hf}(\rho_{eh})m^*_{opt}(\rho_{eh})}, \qquad (4)$$

where the effective optical (e–h pair) mass $m^*_{opt} \approx 0.14$ [15, 17, 19, 20, 51] is a ρ_{eh}-dependent quantity, varying with the transient band filling due to band dispersion and with the bandgap renormalization [57].

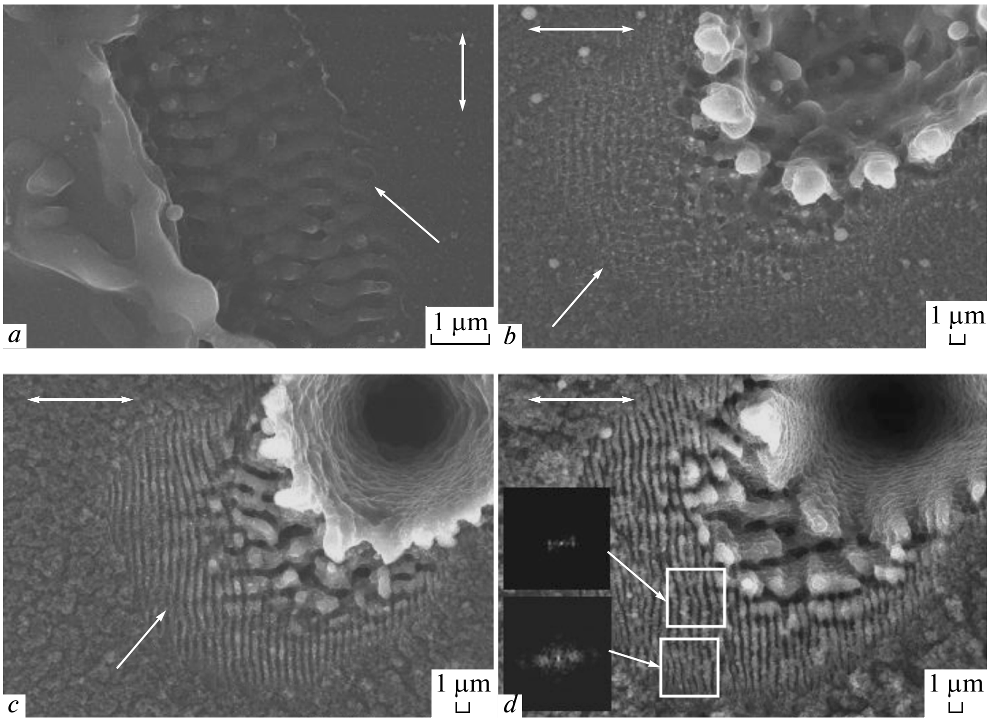

Fig. 5. SEM images of peripheral ripples around ablative craters on the silicon surface generated by 515 nm (a — 2.5 eV, $F = 0.45$ J/cm^2, $N = 3$) and 1030 nm (b–d — 1.25 eV, $F = 1$ J/cm^2, $N = 30$, 100, 300) fs-laser pulses, with the squares showing the 2D fast fourier transform spectra of the corresponding surface spots in the light frames. The bilateral arrows show the laser polarization, while the unilateral ones indicate the surface ripples

The high-frequency electronic dielectric constant ε_{hf} was modeled in the form $\varepsilon_{hf}(\rho_{eh}) = 1 + \varepsilon_{hf}(0) \times \exp(-\rho_{eh}/\rho_{scr})$, where the screening density $\rho_{scr} \approx 1 \cdot 10^{21}$ cm^{-3} was chosen to ensure that $\varepsilon_{hf} \to 1$ in a dense EHP. The electronic damping time τ_e in a dense EHP at the probe frequency ω_{pr} was taken, similarly to metals, in the random phase approximation to be proportional to the inverse bulk EHP frequency ω_{pl}^{-1} [58]:

$$\tau_e = \frac{128E_F^2}{\pi^2\sqrt{3}\,\omega_{pl}}\,\frac{1+\exp(-\hbar\omega_{pr}/k_BT_e)}{(\pi k_BT_e)^2+(\hbar\omega_{pr})^2}, \tag{5}$$

where $E_F \approx 1$–2 eV is the effective Fermi-level quasi-energy for electrons and holes at $\rho_{eh} < 1 \cdot 10^{22}$ cm^{-3}, $\hbar$ and k_B are the reduced Planck and Boltzmann constants, and T_e is the unified EHP temperature, which is a weak function of ρ_{eh} [24]. In this paper, the last relation was evaluated for $\hbar\omega_{pr} > k_BT_e$ in the form $\tau_e(\rho_{eh}) \approx 3 \cdot 10^2/\left(\omega_{pl}(\rho_{eh})(\hbar\omega_{pr})^2\right)$, accounting for multiple carrier scattering paths for three top valence subbands, and multiple L- and X-valleys in the lowest conduction band.

The ρ_{eh}-dependent normal-incidence probe reflectivity $R(\rho_{eh})$ calculated using a common Fresnel formula and accounting for all basic effects (bandgap renormalization, band filling, and the EHP screening of the ion core potential [11, 14, 15]) fits well the experimental reflectivity dependences $R(F)$ at $\Delta t = +0.2$ ps ("effective" $\Delta t = +0.1$ ps) in Fig. 2d, demonstrating the characteristic initial dip and the subsequent rise. By contrast, the separate intraband-transition (Drude) term presents a monotonically decreasing trend, which reproduces well the experimental curve near the dip (if the EHP screening effect is taken into account), but fails to provide the subsequent reflectivity rise in the given range of ρ_{eh} magnitudes. Likewise, the pure interband-transition term, varying presumably in the form of "red spectral shifting" due to the prompt electronic bandgap renormalization, provides unsatisfactory fitting of the dip, if the related band filling effect is not accounted for at lower ρ_{eh}. For example, the intermediate reflectivity maximum in Fig. 2d appears at $\rho_{eh} \sim 1 \cdot 10^{21}$ cm^{-3} $\sim \rho_{bf}(L)$ on the corresponding model curve, resulting from the probing of the red-shifted L-valleys of the E_1-band (cf. the reflectivity

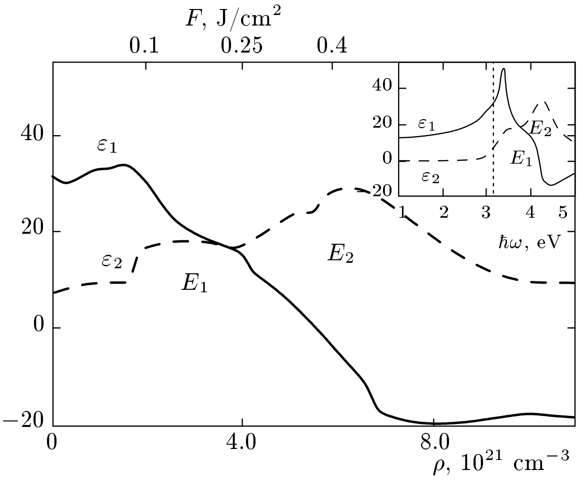

Fig. 6. Dependences of real (ε_1, continuous curve) and imaginary (ε_2, dashed curve) ODF components on ρ_{eh} and F at the 400 nm probe wavelength, showing their red spectral shifts across the E_1 and E_2 bands due to the electronic bandgap shrinkage on a photo-excited Si surface. Inset: spectra of ε_1 and ε_2 for unexcited Si are given for comparison, with the probe photon energy shown by the vertical dotted line

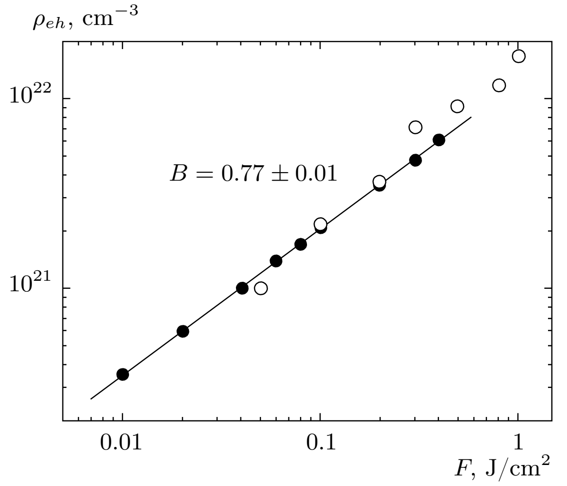

Fig. 7. $\rho_{eh}(F)$ dependences acquired from the reflectivity measurements (dark circles) and numerical modeling (light circles), with the former curve revealing the sublinear trend (proportional to $F^{0.77\pm0.01}$) with the power slope $B = 0.77 \pm 0.01$

spectrum $R(\hbar\omega)$ of silicon in the inset in Fig. 2*a*), if the band-filling effect is neglected. Also, in the dip region, the pure interband-transition term itself yields a very minor reflectivity depression to 0.485 (see the $R(\hbar\omega)$ curve), while the major depression comes from the Drude term enhanced by the EHP screening of ion–core potentials. Meanwhile, the subsequent reflectivity increase to 0.67 is related primarily to the "red spectral shifting" effect with the final reflectivity saturation matching the UV reflectivity plateau for unexcited Si across the E_2-band (cf. the $R(\hbar\omega)$ curve). But because the prompt electronic maximum bandgap renormalization is limited by 50 % (i. e., by $\delta E_{G,e} \approx 1.7$ eV), the maximum effective probe energy approaches 4.8 eV exactly at the beginning of the plateau. Then the subsequent expected increase in ρ_{eh} with F would support not a larger electronic bandgap renormalization but even a lower one [10, 14] and the increasing Drude contribution. However, this is not the case in our experiments (Fig. 2*d*), as is discussed in terms of the EHP dynamics below.

The experimentally derived real and imaginary ODF components at the probe frequency as functions of ρ_{eh} exhibited a monotonically decreasing negative real part ε_1 and a monotonically increasing imaginary part ε_2 (Fig. 6). Such dropping ε_1 and rising ε_2 magnitudes represent characteristic "red-shift" changes of these quantities across absorption bands in strongly photo-excited semiconductors due to their prompt ρ_{eh}-dependent bandgap renormalization [11–15], where the well-known E_1 and E_2 bands of silicon are prominent in Fig. 6 (cf. the inset in Fig. 6). The reasonable fitting of the experimental reflectivity data by means of the presented model ODF allows applying it to ODF simulations for strongly photo-excited silicon at other fs-laser wavelengths and calculating its surface plasmon–polariton dispersion curves.

Furthermore, the fitting results in Fig. 2*d* provide an important relation between the magnitudes of ρ_{eh} and F in the region covering the reflectivity dip and rise. When plotted as $\rho_{eh}(F)$, this relation reveals a sublinear trend proportional to $F^{0.77\pm0.01}$ (Fig. 7), which can be understood by considering a simple kinetic model of the EHP dynamics during the 100 fs laser pump pulse [14, 24]

$$\partial\rho_{eh}/\partial t \approx G\left(I(t)\right) - \gamma(\rho_{eh})\rho_{eh}^3, \tag{6}$$

with the first intensity-dependent photo-ionization term and the second nonlinear limiting Auger recombination term (the coefficient γ is a nonlinear function of ρ_{eh}, rapidly increasing at $\rho_{eh} \sim \rho_{bgr}$ [14]), while the EHP ambipolar diffusion into bulk Si is negligible on the 100 fs pump pulse scale over the energy deposition depth of about 10^{-5} cm. First, there is a strong-excitation steady-state regime with the dense EHP ($\rho_{eh} > 10^{21}$ cm^{-3}) resulting from the counterbalanced ionization and recombination rates $G(I(t)) \approx \gamma(\rho_{eh})\rho_{eh}^3$. This yields the relation $\rho_{eh} \propto F^{2/3}$ at moderate $\rho_{eh} < \rho_{bgr}$ in the case of the interband two-photon absorption (TPA) process, which is allowed for valence-to-conduction band transitions by the corresponding selection rules [35] and predominates during EHP generation in silicon in the IR and visible ranges [6, 18]. Indeed, at the TW/cm^2-level peak fs-laser intensities, the TPA-based absorption with the TPA coefficient $\beta \sim 1$–10 cm/GW [6, 18] becomes much stronger ($\alpha_2 \sim 10^4$–10^5 cm^{-1}) than the tabulated indirect single-photon absorption with the coefficient $\alpha_{1ind} \sim 10^3$–10^4 cm^{-1}) [5]. Second, there is a weak excitation unsteady-state regime, when almost unlimited TPA-based ionization proceeds during the laser pulse, gradually increasing ρ_{eh}. Hence, the experimentally observed exponent $B \approx 0.77 > 2/3$ may reflect the transient convolution of pure TPA ($\rho_{eh} \propto F^2$) at the leading pump pulse front for $\rho_{eh} < 10^{21}$ cm^{-3} with the steady-state Auger-recombination-limited ionization through TPA ($\rho_{eh} \propto F^{2/3}$) for $\rho_{eh} > 10^{21}$ cm^{-3} at later times. A similar fs-laser TPA excitation dynamics in Si with a subsequent drastic rise increase in linear absorption, corresponding to the E_2-band, was earlier observed in a transmission mode for silicon-on-insulator samples at the 2 eV photon energy and lower (less than 1 TW/cm^2) intensities [18].

These experimental finding are well supported by the theoretical modeling results presented as transient ionization/recombination rates and EHP density transients in Figs. 8 and 9, using the derived TPA coefficient β(800 nm) $\approx$ 1.5 cm/GW, which is reasonably consistent with the well-known low-intensity values β(800 nm) $\approx$ 2 cm/GW [6]. At lower intensities $I_L < 1$ TW/cm^2 ($F < 0.1$ J/cm^2), the calculated rates indicate the negligible impact ionization and bandgap renormalization effects with the overall TPA-based ionization rate slightly exceeding the Auger recombination one (Fig. 8*a,b*). In contrast, at higher intensities $I_L > 5$ TW/cm^2 ($F > 0.5$ J/cm^2), the BGR effect visibly promotes all these processes (Fig. 8*c,d*), with the impact ionization rate significantly increasing, but still remaining negligible compared to the TPA rate, while the corresponding Auger recombination rate increases even more, tending to the TPA one. As a result, the calculated magnitudes ρ_{eh} vary sublinearly as functions of I_L (Figs. 7, 9), providing a pronounced BGR $\sim$ 0.1–1 eV and the related BGR-induced increase in ρ_{eh} at higher densities, more than 10^{21} cm^{-3} (Fig. 9*b,c,d*). Finally, the calculated density transients demonstrate slow variation in the maximum at the pump end ($t \approx +0.5\tau_L$), with the steep preceding accumulative EHP dynamics and its more smooth succeeding relaxation dynamics. This justifies our choice of the delay instant $\Delta t = +0.2$ ps as the effective "pump-pulse end" for the acquisition of the peak EHP density at different photoexcitation levels.

Interestingly, the probing at the SH photon energy allows relating the observed saturation ("bleaching") of the interband $L \rightarrow L$ transitions at the probe energy (Fig. 2*d*) to the corresponding TPA-pumping at the fundamental photon energy. According to the electronic capacity of about $4 \cdot 10^{21}$ cm^{-3} of the four relevant L-valleys in Si [51], their band filling simultaneously provides a prompt isotropic bandgap renormalization by approximately 0.7 eV, spectrally shifting the TPA pumping and SH probing across the spectral E_1-band to the red shoulder of the higher-energy E_2 band, exactly as experimentally observed in the form of the probe reflectivity rise and its plateau in Fig. 2*d*. In comparison to these prompt electronic processes, intervalley L–X transfer occurs on a longer time scale (to about 180 fs [60]), not directly affecting the photoexcitation of X-valleys.

5.2. Relief ripples as imprints of instantaneous plasmon–polaritons on photo-excited Si surfaces

Surface relief nanogratings (ripples) emerge on photo-excited material surfaces via multi-shot fs-laser periodical local ablation, occurring at periodical maxima of the deposited volume energy density in the surface layer (the "interference" nanostructuring mechanism [23, 52]). In this mechanism, energy density maxima on a surface result from constructive interference of a tangential component of a transverse fs-laser electric field and of a longitudinal surface plasmon–polariton (SPP) electric field, where the surface plasmon–polaritonic wave is promptly excited during the fs-laser pulses at the same frequency ω, but at a different wavenumber $k = k_1 + ik_2$ accounting for the effective refractive index of the photo-excited material surface [42]. Hence, the experimentally observed surface ripples represent permanent surface imprints of transient SPP waves and, hence, can be used to reveal the underlying SPP modes.

To make such SPP identification possible, the model ODF in Eq. (3), accounting for the complete set of prompt electronic processes with their basic parameters justified by time-resolved reflectivity studies, was used to simulate a number of dispersion relations $\hbar\omega$–k_1 (Fig. 10) for SPPs on fs-laser photo-excited Si surfaces at different values $\rho_{eh} = (1$–$8) \cdot 10^{21}$ cm^{-3}.

Here, the SPP dispersion relations $\hbar\omega$–k_1; for pho-

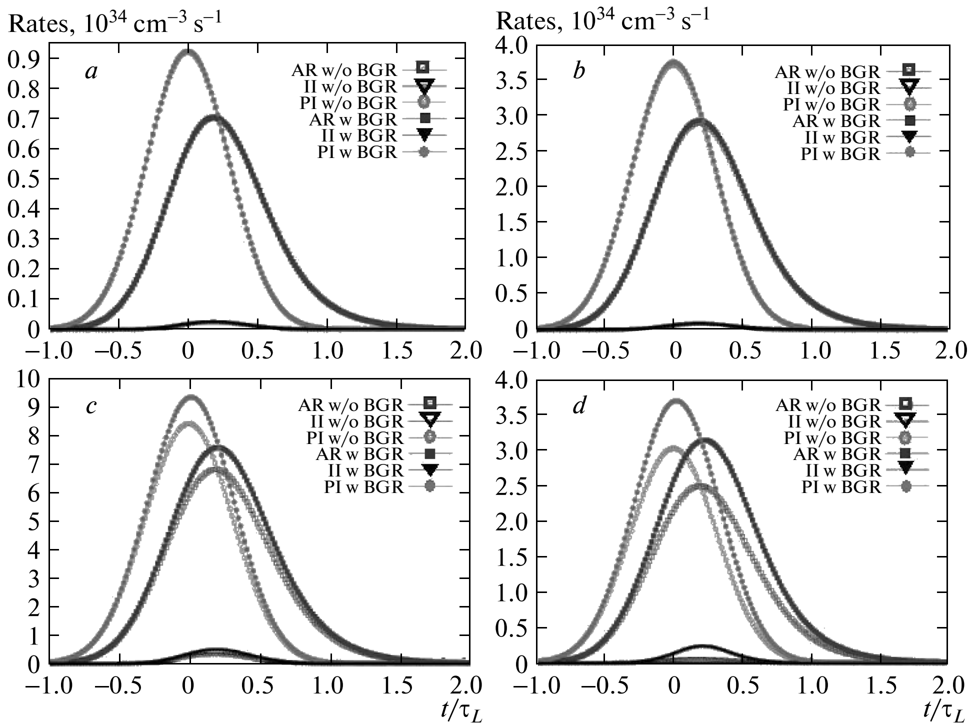

Fig. 8. Calculated transients of photo-ionization (PI), impact ionization (II), and Auger recombination (AR) rates for the low-intensity weak-BGR regime at $I_L = 0.5$ (*a*), 1 TW/cm^2 (*b*), medium-intensity, intermediately strong BGR regime at 5 TW/cm^2 (*c*), and high-intensity, strong BGR regime at 10 TW/cm^2

toexcited silicon were calculated using the common equation [23, 42, 52]

$$k = \nu\sqrt{\frac{\varepsilon\eta}{\varepsilon+\eta}}\,, \tag{7}$$

where ν is the inverse wavelength in vacuum, and $\varepsilon = \varepsilon_1 + i\varepsilon_2$ and $\eta = \eta_1 + i\eta_2$ are the respective frequency-dependent dielectric functions of the plasmon-active metallic (strongly photo-excited silicon) and inactive dielectric (air) boundary media. In order to simulate complete SPP dispersion curves in the broad range of ODF variation depending on ρ_{eh} and $\hbar\omega$, especially, the regime $|\varepsilon_1| < \varepsilon_2$ describing the surface plasmon resonance (SPR) region of such dispersion curves (Fig. 10), which is beyond the commonly used approximation $|\varepsilon_1| \gg \varepsilon_2$ [42], full equations for SPP wave-vector components were used in the very general form [43]

$$k_1 = \nu\sqrt{(1/2D)\left(A+\sqrt{A^2+B^2}\right)}, \quad k_2 = \frac{2\pi\nu^2 B}{2Dk_1}, \tag{8}$$

with [43]

$$\begin{aligned} A &= \eta_1(\varepsilon_1^2+\varepsilon_2^2)+\varepsilon_1(\eta_1^2+\eta_2^2),\\ B &= \eta_2(\varepsilon_1^2+\varepsilon_2^2)+\varepsilon_2(\eta_1^2+\eta_2^2),\\ D &= (\eta_1+\varepsilon_1)^2+(\eta_2+\varepsilon_2)^2. \end{aligned} \tag{9}$$

Additionally, the SPP electric field attenuation coefficient κ, representing the real part of the SPP wave-vector normal component inside the photo-excited Si, was calculated as [43]

$$\kappa = \nu\sqrt{\frac{(\varepsilon_1^2-\varepsilon_2^2)\varepsilon_1+2\varepsilon_1\varepsilon_2^2+(\varepsilon_1^2+\varepsilon_2^2)\sqrt{D}}{2D}} \tag{10}$$

and was used to evaluate spectral amplitudes of the electric field localization factor $L(\hbar\omega) = \kappa(\hbar\omega)/\kappa(\hbar\omega_{pump})$, being normalized here to the attenuation coefficient at the pump energy $\hbar\omega_{pump}$. The localization factor $L(\hbar\omega)$ indicates relative spectral efficiencies of the electric field localization on the photo-excited silicon surface, which is highly important for fs-laser surface nanostructuring in the "interference" regime.

The resulting dispersion curves in Fig. 10 in the range $\rho_{eh} = (1–8)\cdot 10^{21}$ cm^{-3} demonstrate a monotonic blue spectral shift (from the mid-IR to UV range)

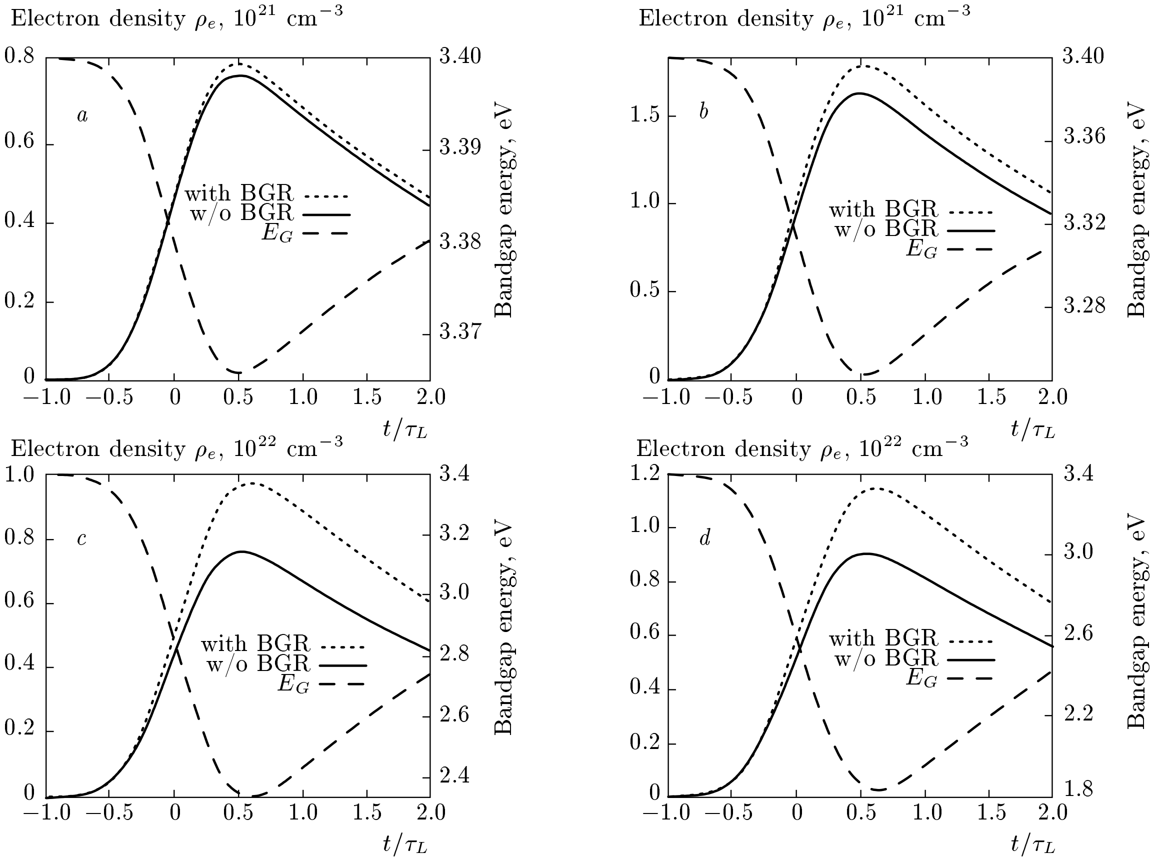

Fig. 9. Calculated transients of the EHP density with the BGR effect included (dotted curve) or excluded (continuous curve), and the direct bandgap E_G at different laser intensities $I_L = 0.5$ (*a*), 1 (*b*), 5 (*c*), 10 (*d*) TW/cm^2

of their SPRs, appearing for each given photon energy in a threshold-like manner, where the threshold condition can be written in terms of ODF as $\varepsilon_1 = -1$ for $\eta = 1$ in air [42]. Each SPR position corresponding to the extreme (zone-edge) wave number $k_\infty = \max\{k_1\}$ tends to higher values k_∞ with increasing ρ_{eh} (Fig. 10). The predicted ultimate values k_∞ at 1030 nm (approximately 1.8 μm^{-1}) and 744 nm (approximately 2.15 μm^{-1}) pump wavelengths are well consistent with the minimal nanoripple periods $\Lambda_{1030,min} \approx 0.55$ μm and $\Lambda_{744,min} \approx 0.42$ μm in Figs. 4 and 5 (curves *3* and *4* in Fig. 10), experimentally observed along the periphery of the nanostructured surface region, i. e., at the very nanostructuring threshold. Likewise, the corresponding minimal values of k_1, lying on the light cone line for the photo-excited material (see the composite inclined straight line in Fig. 10) and, hence, representing the longer-wavelength photonic-like (polaritonic) modes, are also in good agreement with the maximal ripple periods about 1.0 μm at 1030 nm and about 0.65 μm at 744 nm observed at higher laser fluences, i. e., under conditions of stronger photo-excitation. Indeed, each experimental data point in Fig. 10 representing wavenumbers of surface nanogratings at each given laser photon energy $\hbar\omega$ undermines its specific photo-excitation conditions and should be characterized by its individual dispersion curve, which resembles one of the present curves at similar photo-excitation conditions. Furthermore, the corresponding calculated SPR amplitude $K = \max\{k_2\}$, characterizing the longitudinal attenuation coefficient (SPR Q-factor), initially increases with ρ_{eh} (Fig. 11), demonstrating much stronger narrow resonances for more dense EHP. Finally, the localization factor $L(\hbar\omega)$ exhibits the initial increase near each SPR (Fig. 12), indicating the increasing efficiency of fs-laser surface nanostructuring via the "interference" mechanism, which is about one order of magnitude more efficient in terms of acting electric fields if surface plasmonic (SPR) rather than polaritonic modes are involved in such surface nanostructuring.

However, all the abovementioned quantities vary nonmonotonically over the entire range $\rho_{eh} = (1–8) \times 10^{21}$ cm^{-3}, eventually diminishing at higher ρ_{eh} (Figs. 10–12). In particular, the surface plasmon reso-

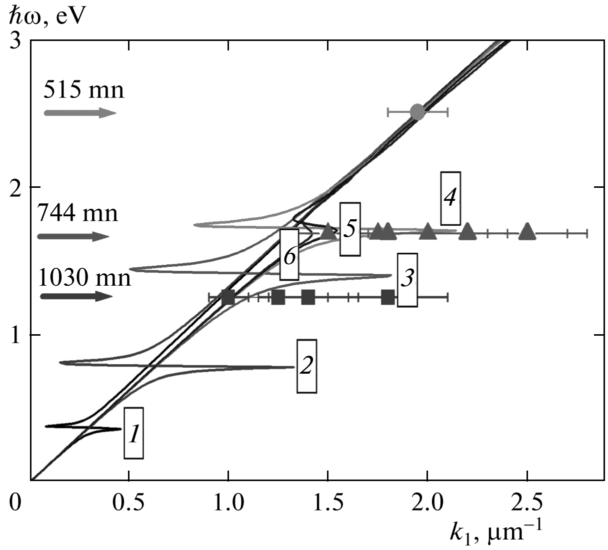

Fig. 10. SPP dispersion curves $\hbar\omega$–k_1 for photo-excited Si surfaces at different ρ_{eh} [$\times 10^{21}$ cm^{-3}]: 1 (*1*), 2 (*2*), 4 (*3*), 6 (*4*), 7 (*5*), and 8 (*6*), with the color arrows showing the 1030 nm, 744 nm, and 515 nm pump photon energies and corresponding colored symbols showing the observed surface ripple wave numbers at various N and F

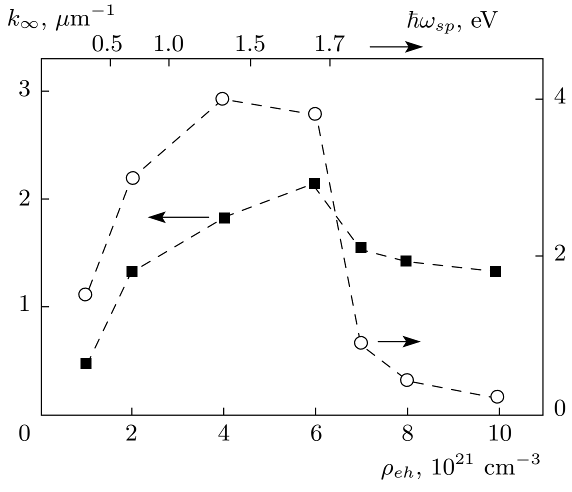

Fig. 11. Basic SPR characteristics — the maximum wave numbers k_∞ (dark squares, left axis) and K (light circles, right axis) — versus ρ_{eh} (bottom axis) on a photo-excited Si surface. The upper axis shows the correspondence between the surface plasmon energy $\hbar\omega_{sp}$ and ρ_{eh}

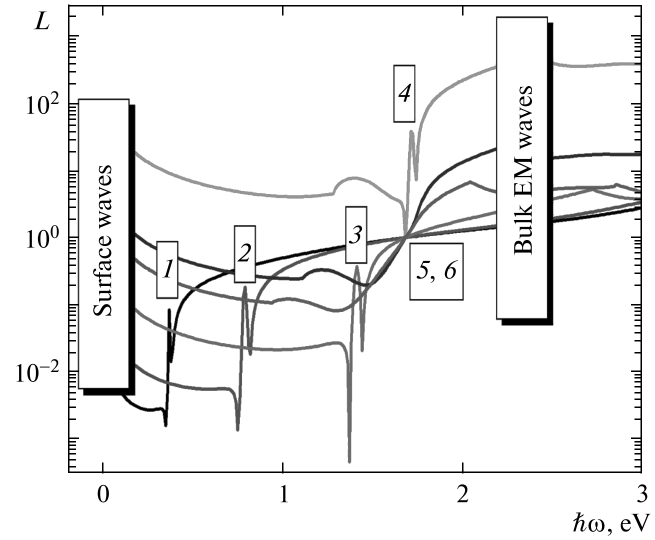

Fig. 12. Spectra of the normalized field localization factor L for photo-excited silicon at $\rho_{eh} = 1$, 2, 4, 6, 7, $8\cdot 10^{21}$ cm^{-3}, respectively shown by the *1*, *2*, *3*, *4*, *5*, and *6* curves, with corresponding numbers indicating their sharp surface plasmon resonances. Surface and bulk electromagnetic waves exist in the regions to the left and to the right of the resonances, indicated by the numbers *1*–*6*

nances are very pronounced only for $\hbar\omega < 1.7$ eV, since the critical photoexcitation with $\rho_{eh} > 6\cdot 10^{21}$ cm^{-3}, which is required to make the material plasmonic, shifts these resonances toward the red shoulder of the absorption E_1 band in silicon with its peak at 3.4 eV [5]. This occurs when such dense EHP provides a significant prompt electronic bandgap renormalization (spectral "red" shift) by $\delta E_{G,e} \approx \Theta\rho_{eh}/\rho_{bgr} > 1$ eV (where $\Theta/\rho_{bgr} \approx 1.7\cdot 10^{-22}$ eV/cm^3), making the actual photon energy $\hbar\omega \approx 1.7$ eV larger by $\delta E_{G,e}$ and tuning the resulting effective pump photon energy to 3.4 eV at the red shoulder of the absorption E_1 band. As a result of significant interband absorption within the band, SPRs of photo-excited Si become strongly broadened and damped (Fig. 10). Similarly, the localization factor $L(\hbar\omega)$ and the SPR amplitude K drop significantly due to the increased interband absorption losses at the E_1 band (Figs. 11 and 12). Moreover, at higher $\hbar\omega > 1.7$ eV, the prompt electronic bandgap renormalization owing to dense EHP shifts the SPR even deeper to the spectral region of strong interband absorption, related to the E_1 and E_2 bands of the material [5]. Hence, the advantageous continuous sub-bandgap tunability of silicon, as an example of other virtual plasmonic materials, in terms of simultaneous spectral SPR tuning and electric field localization exhibits intrinsic limits, related to intense above-gap interband absorption losses.

Importantly, during the 100 fs laser pump pulse, the highly efficient targeted SPR excitation on silicon surfaces becomes possible at a particular pump photon energy $\hbar\omega_{las} < 1.7$ eV, when the temporal EHP density saturation occurs in the Auger recombination-controlled regime at the appropriate density level ρ_{eh} (cf. Figs. 7 and 9), tuning the resonance to this particular energy $\hbar\omega_{las}$ at the given peak laser intensity. This EHP density level is a threshold one for the photon energy $\hbar\omega_{las}$, since SPP excitation is not possible at lower magnitudes ρ_{eh}, while higher values of ρ_{eh} shift the resonance up, enabling photoexcitation of presumably low-field, lower-k_1 photonic-like (polaritonic) SPP modes (Fig. 10). In the latter case, SPR excitation may occur only for a short time, when the SPR is tuned across the fs-laser bandwidth, i. e., the overall SPR excitation is not efficient compared to the above-mentioned polaritonic modes.

Surprisingly, despite the evident possibility of SPR excitation during fs-laser surface nanostructuring, its nonpropagating ($\omega/k_1 \to 0$), strongly dissipative (high k_2-amplitudes) character makes its use challenging to fabricate regular surface ripples, if such excitation occurs on spontaneous surface roughness. One can assume that multiple nanostructured domains should emerge on a sample surface under SPR excitation conditions owing to multiple and chaotic light scattering centers. Meanwhile, in Figs. 4 and 5 in this paper, we demonstrate multi-micron regions covered by SPR-induced surface ripples, becoming possible, apparently, due to other, nonlinear SPP excitation mechanisms (e. g., due to fs-laser driven "optical roughness" [60]).

6. CONCLUSIONS

In conclusion, prompt optical constants of an fs-laser photo-excited silicon surface and related electron–hole plasma dynamics were experimentally acquired by means of time-resolved optical reflection microscopy and numerically modeled using a quantum kinetic approach. The gained knowledge of the prompt optical dielectric function of the photo-excited material enabled simulating its SPP dispersion curves at different electron–hole plasma densities, predicting nonmonotonic tunability, and positions and amplitudes of their surface plasmon resonances in the sub-bandgap spectral range. These theoretical results are supported by direct experimental multi-color mapping of the dispersion curves at several laser photon energies, achieved by measuring spatial periods of the corresponding SPP-mediated surface relief nanogratings. Vice versa, the gained electronic dynamics and SPP dispersion curves indicate SPP modes favorable for fs-laser surface nanostructuring, and enlighten related promising fabrication regimes.

The authors acknowledge financial support from the RAS Presidium (Program No. 24) and from the Russian Foundation for Basic Research (grant No. 13-02-00971).

REFERENCES

1. A. V. Krasavin and A. V. Zayats, Opt. Express **18**, 11791 (2010).

2. A. B. Pevtsov, D. A. Kurdyukov, V. G. Golubev, A. V. Akimov, A. A. Meluchev, A. V. Sel'kin, A. A. Kaplyanskii, D. R. Yakovlev, and M. Bayer, Phys. Rev. B **75**, 153101 (2007).

3. Y. C. Shen, P. C. Upadhya, E. H. Linfield, H. E. Beere, and A. G. Davies, Appl. Phys. Lett. **83**, 3117 (2003).

4. A. Urbanowicz, A. Krotkus, R. Adomavičius, and V. L. Malevich, Physica B **398**, 98 (2007).

5. E. D. Palik, *Handbook of Optical Constants of Solids*, Academic Press, Orlando (1998).

6. A. D. Bristow, N. Rotenberg, and H. M. van Driel, Appl. Phys. Lett. **90**, 191104 (2007).

7. A. J. Sabbah and D. M. Riffe, Phys. Rev. B **66**, 165217 (2002).

8. K. F. Berggren and B. E. Sernelius, Phys. Rev. B **24**, 1971 (1981).

9. A. Oschlies, R. W. Godby, and R. J. Needs, Phys. Rev. B **45**, 13741 (1992).

10. C. D. Spataru, L. X. Benedict, and S. G. Louie, Phys. Rev. B **69**, 205204 (2004).

11. E. N. Glezer, Y. Siegal, L. Huang, and E. Mazur, Phys. Rev. B **51**, 6959 (1995).

12. S. I. Kudryashov and V. I. Emel'yanov, JETP **94**, 94 (2002).

13. S. I. Kudryashov, M. Kandyla, C. A. D. Roeser, and E. Mazur, Phys. Rev. B **75**, 085207 (2007).

14. T. Apostolova, A. A. Ionin, S. I. Kudryashov, L. V. Seleznev, and D. V. Sinitsyn, Opt. Eng. **51**, 121808 (2012).

15. A. A. Ionin, S. I. Kudryashov, S. V. Makarov, P. N. Saltuganov, L. V. Seleznev, D. V. Sinitsyn, and A. R. Sharipov, JETP Lett. **96**, 375 (2012).

16. C. V. Shank, R. Yen, and C. Hirlimann, Phys. Rev. Lett. **50**, 454 (1983).

17. D. Hulin, M. Combescot, J. Bok, A. Migus, J. Y. Vinet, and A. Antonetti, Phys. Rev. Lett. **52**, 1998 (1984).

18. D. H. Reitze, T. R. Zhang, Wm. M. Wood, and M. C. Downer, J. Opt. Soc. Amer. B **7**, 84 (1990).

19. K. Sokolowski-Tinten and D. von der Linde, Phys. Rev. B **61**, 2643 (2000).

20. T. Y. Choi and C. P. Grigoropoulos, J. Appl. Phys. **92**, 4918 (2002).

21. J. Bonse, Appl. Phys. A **84**, 63 (2006).

22. M. B. Agranat, S. I. Ashitkov, S. I. Anisimov, and A. V. Ovchinnikov, Appl. Phys. A **94**, 879 (2009).

23. S. A. Akhmanov, V. I. Emel'yanov, N. I. Koroteev, and V. N. Seminogov, Sov. Phys. Usp. **28**, 1084 (1985).

24. E. J. Yoffa, Phys. Rev. B **21**, 2415 (1980).

25. N. M. Bulgakova, R. Stoian, A. Rosenfeld, I. V. Hertel, and E. E. B. Campbell, Phys. Rev. B **69**, 054102 (2004).

26. T. J. Derrien, T. Sarnet, M. Sentis, and T. E. Itina, J. Optoelectronics Adv. Mater. **12**, 610 (2010).

27. H. M. van Driel, Phys. Rev. B **35**, 8166 (1987).

28. J. K. Chen, D. Y. Tzou, and J. E. Beraun, Int. J. Heat Mass Transfer **48**, 501 (2005).

29. T. J. Derrien, J. Krueger, T. E. Itina, S. Hoehm, A. Rosenfeld, and J. Bonse, Opt. Express **24**, 29643 (2013).

30. Y. Gan and J. K. Chen, Comp. Phys. Comm. **183**, 278 (2012).

31. L. D. Pietanza, G. Colonna, S. Longo, and M. Capitelli, Eur. Phys. J. D **45**, 369 (2007).

32. N. S. Shcheblanov and T. E. Itina, Appl. Phys. A **110**, 579 (2013).

33. N. Medvedev, U. Zastrau, E. Forster, D. O. Gericke, and B. Rethfeld, Phys. Rev. Lett. **107**, 165003 (2011).

34. V. Laporta, L. D. Pietanza, and G. Colonna, Nucl. Instr. Meth. Phys. Res. A **636**, 67 (2011).

35. S. I. Kudryashov, SPIE **5448**, 1171 (2004).

36. R. Wagner, J. Gottmann, A. Horn, and E. W. Kreutz, Appl. Surf. Sci. **252**, 8576 (2006).

37. T. H. R. Crawford and H. K. Hagen, Appl. Surf. Sci. **253**, 4970 (2007).

38. M. Huang, F. Zhao, Y. Cheng, N. Xu, and Z. Xu, ACS Nano **3**, 4062 (2009).

39. J. Bonse, A. Rosenfeld, and J. Krueger, J. Appl. Phys. **106**, 104910 (2009).

40. O. Varlamova, F. Costache, J. Reif, and M. Bestehorn, Appl. Surf. Sci. **252**, 4702 (2006).

41. A. A. Ionin, S. I. Kudryashov, S. V. Makarov, L. V. Seleznev, D. V. Sinitsyn, E. V. Golosov, O. A. Golosova, Yu. R. Kolobov, and A. E. Ligachev, Quant. Electr. **41**, 829 (2011).

42. S. A. Maier, *Plasmonics: Fundamentals and Applications*, Springer, Berlin (2007).

43. R. J. Bell, R. W. Alexander, Jr., W. F. Parks, and G. Kovener, Opt. Comm. **8**, 147 (1973).

44. A. Couairon and A. Mysyrowicz, Phys. Rep. **441**, 47 (2007).

45. T. Apostolova, D. Huang, P. Alsing, J. McIver, and D. A. Cardimona, Phys. Rev. B **66**, 075208 (2002).

46. A. Haug, Phys. Stat. Sol. (b) **108**, 443 (1981).

47. T. Apostolova, D. H. Huang, P. M. Alsing, and D. A. Cardimona, Phys. Rev. A **71**, 013810 (2005).

48. J. H. Bechtel and W. L. Smith, Phys. Rev. B **13**, 3515 (1976).

49. W. Lochmann, Phys. Stat. sol. (a) **45**, 423 (1978).

50. D. B. Laks, G. F. Neumark, and S. T. Pantelides, Phys. Rev. B **42**, 5176 (1990).

51. A. Dargys and J. Kundrotas, *Handbook on Physical Properties of* Ge, Si, GaAs *and* InP, *Science and Encyclopedia Publishers*, Vilnius (1994).

52. J. E. Sipe, J. F. Young, J. S. Preston, and H. M. van Driel, Phys. Rev. B **27**, 1141 (1983).

53. J. Bonse, M. Munz, and H. Sturm, J. Appl. Phys. **97**, 013538 (2005).

54. J. Bonse and J. Krueger, J. Appl. Phys. **108**, 034903 (2010).

55. A. A. Ionin, Y. M. Klimachev, A. Y. Kozlov, S. I. Kudryashov, A. E. Ligachev, S. V. Makarov, L. V. Seleznev, D. V. Sinitsyn, A. A. Rudenko, and R. A. Khmelnitsky, Appl. Phys. B **111**, 419 (2013).

56. S. Sakabe, M. Hashida, S. Tokita, S. Namba, and K. Okamuro, Phys. Rev. B **79**, 033409 (2009).

57. P. Y. Yu and M. Cardona, *Fundamentals of Semiconductors*, Springer, Berlin (2005).

58. R. H. M. Groeneveld, R. Sprik, and A. Lagendijk, Phys. Rev. B **51**, 11433 (1995).

59. T. Ichibayashi, S. Tanaka, J. Kanasaki, and K. Tanimura, Phys. Rev. B **84**, 235210 (2011).

60. A. A. Ionin, S. I. Kudryashov, L. V. Seleznev, D. V. Sinitsyn, and V. I. Emel'yanov, JETP Lett. **97**, 121 (2013).